5-2013

Direct measurement of through-plane thermal conductivity of partially saturated fuel cell diffusion media

Guoqing Xu
University of Tennessee - Knoxville, gxu4@utk.edu

To the Graduate Council:

I am submitting herewith a thesis written by Guoqing Xu entitled "Direct measurement of through-plane thermal conductivity of partially saturated fuel cell diffusion media." I have examined the final electronic copy of this thesis for form and content and recommend that it be accepted in partial fulfillment of the requirements for the degree of Master of Science, with a major in Mechanical Engineering.

Matthew M. Mench, Major Professor

We have read this thesis and recommend its acceptance:

Rao V. Arimilli, Kivanc Ekici, James Schmidhammer

Accepted for the Council:
Carolyn R. Hodges

Vice Provost and Dean of the Graduate School

(Original signatures are on file with official student records.)

Direct measurement of through-plane thermal conductivity of partially saturated fuel cell diffusion media

A Thesis Presented for the

Master of Science

Degree

The University of Tennessee, Knoxville

Guoqing Xu

May 2013

ACKNOWLEDGEMENTS

To my advisor, Dr. Matthew M. Mench, for giving me the opportunity to work in the lab collaborating with an amazing group of graduate students, postdocs, research professors and administrative staff, and for passing on to me his research, career and cultural experience.

To all the teachers, Dr. Arimilli, Dr. Ekici, Dr. Schmidhammer, Dr. Landes, Dr. Armsworth, and others, for your knowledge, experience, education and support.

To all the graduate students, postdocs, research professors and administrative staffs I have been working with, for their help, encouragement, friendship, insights and unforgettable memories.

To the members of the Navigators at University of Tennessee, Knoxville for their help, friendship and support.

To General Motors for their insight and support.

This work is supported by the US Department of Energy under Award Number *DE-EE0000470*.

ABSTRACT

Polymer electrolyte fuel cells (PEFCs) are predicted by many as the most feasible alternative to heat engines and for battery replacement in automotive, portable, and stationary power applications. Fuel cell performance and durability are inseparably related to the presence of liquid water throughout the fuel cell system. To better understand the mechanical and thermal characterization of diffusion media (DM) is essential to PEFC DM design, optimization and production to improve water and thermal managements. Diffusion media are one of the important components in PEFCs in terms of the reactant permeability, the product permeability, the electronic conductivity, the heat conductivity, and the mechanical strength. Thermal conductivity is a particularly important parameter due to the interplay between heat and water management. The thickness of DM is one of the components that are highly dependable on compression.

In this study, optical microscope was used to investigate the stress strain relationship. Nonlinear sharp increase in strain at initial compressive loading was observed. Thermal conductivity of all dry DM was found to increase with compression. Measured and predicted maximum thermal conductivity as a function of saturation for DM at 2MPa compression was performed. There was a significant increase in thermal conductivity with an increase in saturation. Thermal conductivity as a function of both compression and saturation was developed.

TABLE OF CONTENTS

LIST OF TABLES

LIST OF FIGURES

LIST OF SYMBOLS

Greek:

τ	coefficient of thermal expansion
ρ	density
ξ	volume ratio
ω	weighting
ε	total strain on compressed diffusion media
ε^*	total strain on compressed macroporous layer
ε_0	strain on measured diffusion media
ϕ^*	compressed porosity
ϕ	initial porosity
σ	stress/compression
α	thermal diffusivity

English:

q''	heat flux
k	thermal conductivity
T	temperature
x	distance
Q	heat
l	thickness of diffusion media
A	area
P	power output
t	time
R	resistance
c_p	specific heat
l_0	thickness of measured diffusion media
s	saturation
m	mass

Subscript:

h	hot plate
c	cold plate
t	at time t
dry	dry sample
wet	wet/saturated sample
$water$	water

CHAPTER I

INTRODUCTION AND GENERAL INFORMATION

Polymer Electrolyte Fuel Cells

Back in 1776, when esteemed scientist Henry Cavendish found that water is formed when hydrogen reacts with oxygen. Later on, Dr. Christian Schönbein discovered the principle of the fuel cell in 1838. Today, the science and technology of fuel cell engines are revolutionizing the industry, providing clean, debatable, and reliable energy. The fuel cell technology is being utilized in portable power generation, stationary power generation and power for transportation. Polymer electrolyte fuel cells (PEFCs) are envisioned by many as the most viable alternative to heat engines and for battery replacement in automotive, stationary, and portable power applications [1].

PEFCs operate with hydrogen as the fuel and oxygen in the air to generate electricity from electrochemical reaction at 20-80°C. A typical hydrogen PEFC is mainly composed of backing plates (BPs), diffusion media (DM), microporous layers (MPL), catalyst layers (CL), and membrane. A schematic diagram of hydrogen PEFC is shown in Figure 1. Hydrogen fuel and air are delivered through flow fields in the BPs on the anode and cathode side, respectively. Then, hydrogen and oxygen diffuse through DM and MPL to the CL

on each side. On the anode side, hydrogen molecules are catalytically split into protons and electrons. The protons go through the membrane to the catalyst layer on the cathode side. Meanwhile, the electrons are sent back through MPL, DM, to the external circuit. On the cathode side, oxygen is combined with protons from the anode side and electrons from the external circuit, through DM, and MPL to cathodic CL, producing water.

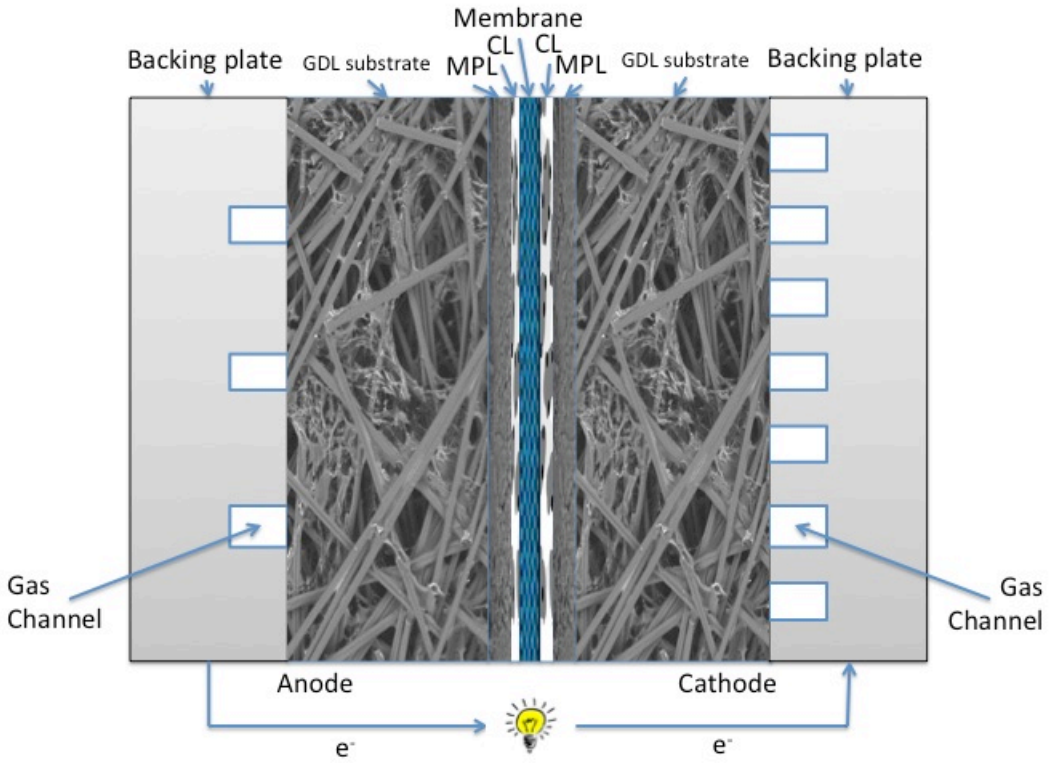

Figure 1. A schematic diagram of hydrogen PEFC

The half cell reactions and overall reaction are listed as follows:

Anodic reaction: $H_2 -> 2H^+ + 2e^-$ (1)

Cathodic reaction: $$\frac{1}{2}O_2 + 2e^- + 2H^+ -> H_2O \quad (2)$$

Overall reaction: $$H_2 + \frac{1}{2}O_2 = H_2O \quad (3)$$

Fuel cell performance and durability are related to the presence of liquid water throughout the fuel cell system. Although some minimum level of saturation is essential to facilitate efficient ionic conductivity in proton exchange membrane, excess liquid water can block CL limiting the power output or fill up pores in DM hindering reactant gas transport [2,3]. A better understanding of the mechanical and thermal properties of diffusion media is essential to PEFC DM design, optimization and production to improve water and thermal managements.

Diffusion Media

Diffusion media are one of the important components in PEFCs in terms of the outstanding characteristics of the reactant permeability, providing reactant gas access from flow-field channels to catalyst layers including in-plane permeability to regions adjacent to lands; the product permeability, providing passage for removal of product water from catalyst-layer area to flow-field channels including in-plane permeability from regions adjacent to lands; the electronic conductivity, providing electronic conductivity from bipolar plates to catalyst layers including in-plane conductivity to regions adjacent to channels; the heat conductivity, providing for efficient heat removal from membrane and CL to

BP where coolant channels are located; and the mechanical strength, providing mechanical support to the membrane and CL in case of reactant pressure difference between the anode and cathode gas channels, maintaining good contact with the MPL and not compressing into channels resulting in blocked flow and high channel pressure drops [4].

Carbon-fiber-based products are the most assuring candidates for the use as DM because of their good electrical conductivity and high porosity, which are generally made of non-woven carbon paper and woven carbon cloth. In order to alleviate flooding, a hydrophobic polymer, Polytetrafluoroethylene (PTFE) is added. Figure 2 presents images of non-woven carbon paper and woven paper cloth from scanning electron microscopy (SEM), respectively.

Porosity of the DM can make the hydrogen fuel and oxygen diffuse to the reaction zones and make produced water removed. Commonly used DM have a porosity range from 70% to 90%. Normally, the DM in a PEFC is deformed under compression under pressures with a range from 1 MPa to 2 MPa or even higher. The cloth DM are generally found to be more compressive than the paper DM. Since thickness and porosity are both dependent on the compression pressure, stress-strain measurement is necessary to be obtained to accurately calculate material properties of DM. Some common properties are given in Table 1. To better predict the temperature distribution in operating PEFCs, through-plane thermal conductivity is of great importance to be measured.

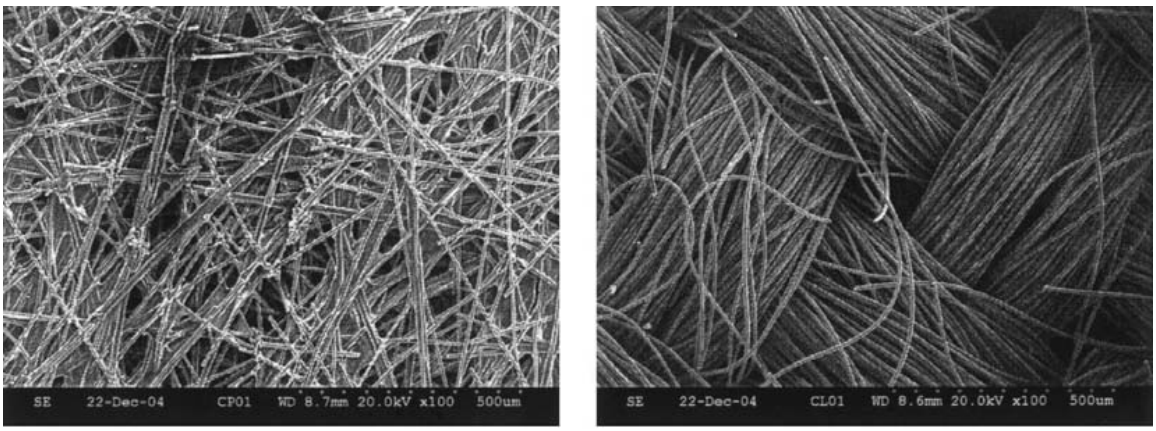

(*a*) (*b*)

Figure 2. SEM of nonwoven fiber paper and woven carbon cloth DM structure: (a) nonwoven fiber; (b) woven carbon cloth. (Image by Soowhan Kim, Penn State Fuel Cell Dynamics and Diagnostics Laboratory.)

Table 1. Common properties of DM

Property	***Cloth DM Value***	***Paper DM Value***
Thickness	250-450 μm	175-450 μm
Porosity	70%-90%	70%-90%
PTFE content (by wt.%, typical)	5-30%	5-30%

Heat conduction, heat convection and heat radiation are three modes of heat transfer. It is well known that DM used in PEFC is a heterogeneous material with carbon fibers or cloth and heat conduction is one dominant heat transfer mode through the DM. For heat conduction, the rate equation is known as Fourier's Law:

$$\vec{q} = -k\nabla T \tag{4}$$

For the one-dimensional case DM with constant thermal conductivity k, the temperature distribution $T(x)$ through DM is shown in Figure 3.

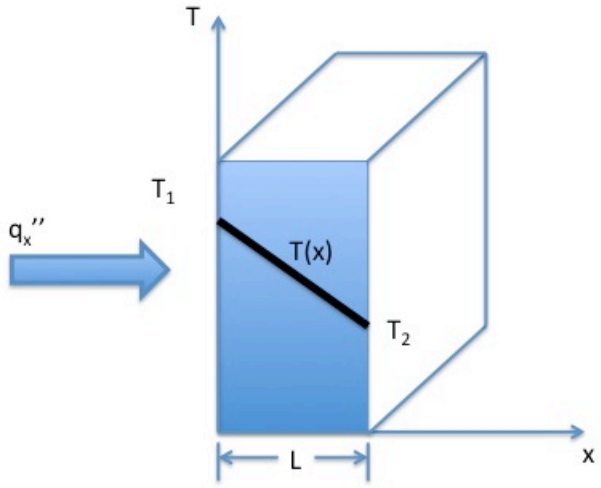

Figure 3. One-dimensional heat conduction

CHAPTER II

LITERATURE REVIEW

Thermal conductivity is a particularly important parameter due to the interplay between heat and water management and dominance of conduction heat transfer in PEFCs. Water generated in PEFCs that condenses into liquid phase must be removed to prevent loss of performance during operation and potential freeze-thaw degradation. PTFE is normally used to improve hydrophobicity of the DM and reduce liquid accumulation. A highly hydrophobic MPL is often utilized between the DM and CL. The MPL is of great importance to alleviate CL flooding, to decrease electrical contact resistance, protect the membrane from damage from DM fibers, and improve membrane hydration. An extensive literature review is done to investigate various experimental approaches for thermal conductivity measurement and different theoretical approaches for thermal conductivity predictions. [5-14]

Heat and Water Management

Normally, an operating PEFC will generate a comparable amount of heat to the power output. The heat generation includes the reversible heat generated

by the entropy change, which is the difference between the thermal and Nernst voltage[1]:

$$q''_{heat,rev}(W/cm^2) = i(E_{th} - E^0) = i(-\frac{\Delta H}{nF} - \frac{\Delta G}{nF}) = -i\frac{T\Delta S}{nF} \quad (5)$$

The irreversible heat generated by activation, ohmic, and concentration polarizations is:

$$q''_{heat,irr}(W/cm^2) = i(E^0 - E_{cell}) = i(\eta_{a,a} + |\eta_{a,c}| + \eta_{m,a} + |\eta_{m,c}| + \eta_R + \eta_x) \quad (6)$$

The total heat generated by reaction polarizations is the sum of the reversible and irreversible components:

$$q''_{total}(W/cm^2) = -i\frac{T\Delta S}{nF} + i(\eta_{a,a} + |\eta_{a,c}| + \eta_{m,a} + |\eta_{m,c}| + \eta_R + \eta_x) \quad (7)$$

Generally, generated heat in PEFC is removed by the cooling system or transferred by conduction and convection. Maintaining a stable temperature in the membrane is challenging since more heat is generated on the cathode side [15-18]. A significant temperature change in the membrane may cause damage through excessive dry out and decrease proton conductivity. Water management is one of the key elements of optimizing PEFCs performance. In order to have high ionic conductivity, the proton exchange membrane must have high water content [19]. However, excess liquid water can block CL limiting the power output or fill up pores in DM hindering reactant gas transport. MPL is used to help with water management. Chuang *et al.* [20] found significant flooding losses at 80°C, 1.5 A/cm^2 current density and eliminated the flooding by increasing the fuel cell

operating temperature up to 85°C. Therefore, a detailed temperature distribution through PEFC is needed to optimize PEFC performance.

Compression

In order to obtain the temperature distribution in PEFC, the thermal conductivity of each component should be determined. The thickness of the DM is one of the components that are highly dependent on compression. In this study, the DM stress-strain relationship was optically measured. The thickness versus compression relationship was then used to calculate the thickness used in the determination of compressed DM thermal conductivity. Moreover, the measured DM stress-strain relationship was used to calculate compressed porosity. As compression increases, pore volume and porosity decreases. The compressed porosity was used to calculate the saturation of DM for thermal conductivity measurement of wet DM. DM materials were determined to suffer irreversible strain of 5-20% from 2.75 MPa compression pressure [4]. Broken up carbon fibers and deteriorated PTFE coating were found in DM under compression using SEM [21]. Different compression in the fuel cell assembly had different performance. J.B. Ge *et al.* [22] found the decrease in fuel cell performance with a increase in compression in 2006.

Experimental approaches for thermal conductivity measurements

Thermal conductivity is a measure of the ability of materials to conduct heat. It is the proportionality factor in Fourier's Law of heat conduction equation. Thermal conductivity of DM varies with temperature, PTFE content, compression and the presence of water content. There are two methods for the measurement of thermal conductivity of DM. These include steady state method and transient method.

The measurement time for steady state method was considered to be too slow for the present application. It takes about twenty minutes to reach steady state condition for the samples under consideration in this study. And this time is too long and unacceptable because the saturation level will not remain constant during the test period.

Transient method does not wait for the signal to be steady. Nevertheless, the signal is recorded as a function of time. The significant advantage of this technique is that the measuring time is much shorter than steady state method and, more importantly, saturation level remains practically constant during the test. In this study, the thermal conductivity will be determined as a function of saturation. Short measuring time will obviously lower the uncertainty in saturation value.

The Tranisent Plane Source (TPS) method, often referred to as "The Gustafsson Probe" in honor of its builder is engineered to non-destructively

measure the thermal conductivity, thermal diffusivity and specific-heat capacity of solid, liquid, paste and powder materials in the range of 0.001 W/mK to 1000 W/mK over temperatures ranging from -160 to 1000°C. Based on the theory of the TPS method, the TPS Thermal Conductivity Analyzer utilizes a sensor element in the shape of a double spiral as seen in Figure 4.

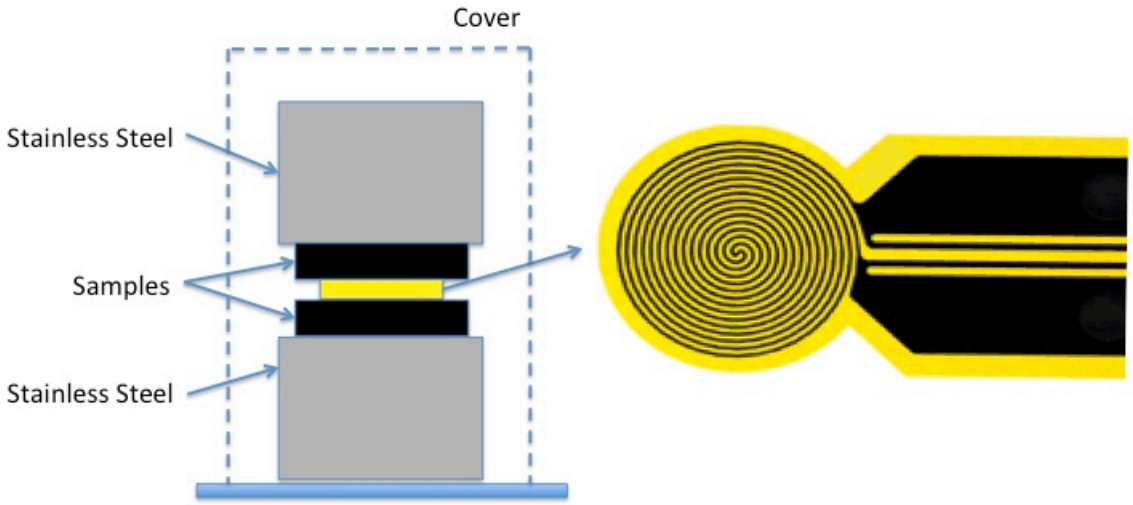

Figure 4. Schematic diagram for Transient Power Source

This TPS sensor functions both as a heat source for increasing the temperature of the sample and a ”resistance thermometer” for recording the transient temperature increases. The sensor element is made of a 10μm thick

Nickel-metal double spiral supported by two 25.4mm thick layers of material to protect its particular shape, give it mechanical strength and keep it electrically insulated. The polyimide film is Kapton, which can be used throughout the temperature range from -160 to 300°C. The encapsulated Ni-spiral sensor is then sandwiched between two halves of the diffusion media. During a pre-set time, 200 resistance recordings are taken, and from these the relation between temperature and time is established. A few parameters, like the "Output of Power" to increase the temperature of the spiral, the "Measuring Time" for recording 200 points and the size of the sensor are used to optimize the settings for the experiment so that thermal conductivities from 0.001 W/mK to 1000 W/mK can be measured. In order to avoid any thin sections of air between the sensor material (Nickel) and the thin insulating sheet as well as between the metal blocks and the sheets, the samples and sensor were firmly clamped together. The thermal conductivity of the thin sample material can then be extracted from the following formula:

$$\frac{P}{2} = Ak\frac{\Delta T}{l} \tag{10}$$

$$\Delta T(t) = \frac{1}{\tau}\left(\frac{R(t)}{R_0} - 1\right) \tag{11}$$

where P is the power output, A is the area of the conducting pattern, k is the thermal conductivity of the thin sample, ΔT is the fully developed temperature difference across one of the insulating layers and l is the thickness of the thin sample pieces, τ is the coefficient of thermal expansion, R_0 and $R(t)$ are the

initial resistance and resistance at time t of the TPS element. Transient temperature will be obtained as shown in Figure 5.

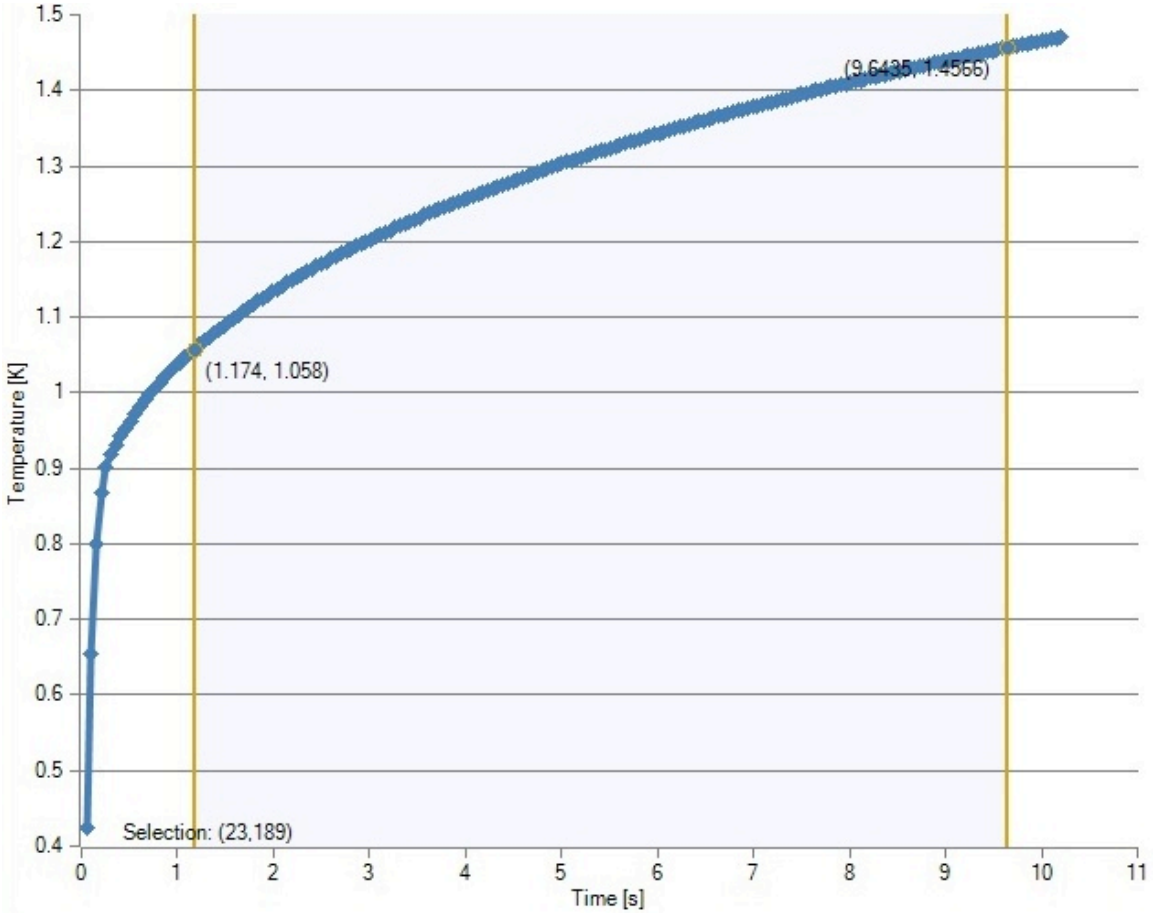

Figure 5. Transient temperature curve

As explained above, the thermal conductivity obtained from these measurements is calculated from the temperature difference between the sensing Nickel pattern and the surface of the stainless steel blocks. This means that we are actually recording the apparent thermal conductivity of all the material that is located between these surfaces. It is obvious that a soft material normally would fill out the volume between the sensor and the stainless steel blocks rather completely,

and the experimental results would then represent the thermal conductivity of the thin sheets or thin films rather well.

The laser flash method has been developed [23-25] to measure through-plane thermal diffusivity of thin films, as illustrated in Figure 6.

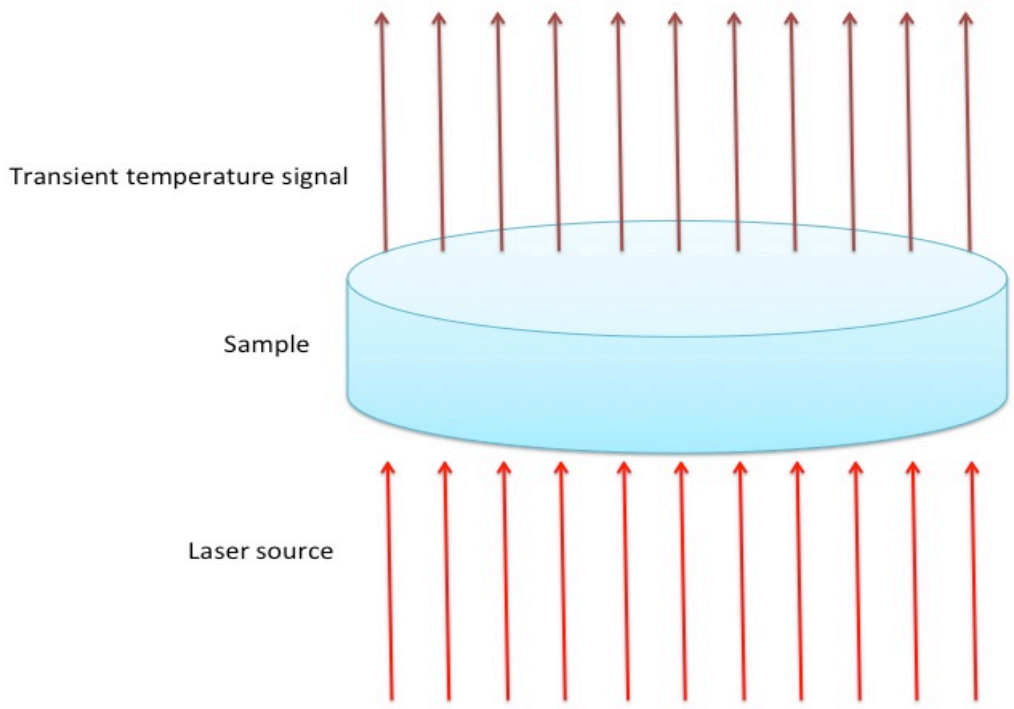

Figure 6. Schematic diagram for Laser Flash Method

One side of the sample is heated by a laser source. Transient temperature rise on the back of the sample is then recorded. The thermal conductivity can be calculated with reference sample specific heat, known sample density, and measured thermal diffusivity:

$$k = \alpha c_p \rho \tag{12}$$

where α is the thermal diffusivity of the sample, c_p is the specific heat of the sample, ρ is the density of the sample.

Jan Zajas *et al.* [26] used the Laser Flash Method to measure the local thermal conductivity of construction materials on a scale of millimeters and created a map of thermal conductivity.

Thermal Conductivity Models

Many models have been described in the literature [8] [27]. The fundamental models used for prediction of thermal conductivity of materials with two components are listed as follows:

1. Parallel model [12]

The parallel model in Figure 7 assumes that both thermal resistances of components are parallel to the heat flow, which will have the maximum thermal conductivity:

$$k = \xi_1 k_1 + \xi_2 k_2 \tag{13}$$

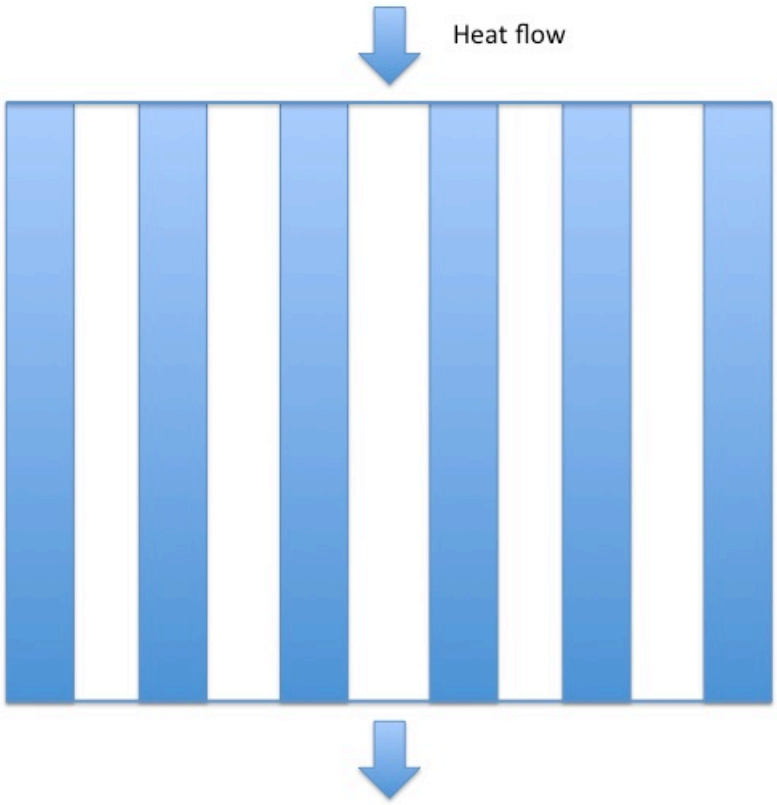

Figure 7. Schematic diagram for parallel model

2. Series model [12]

The series model in Figure 8 assumes that both thermal resistances of components are perpendicular to the heat flow, which will have the minimum thermal conductivity:

$$k = \frac{1}{\frac{\xi_1}{k_1} + \frac{\xi_2}{k_2}} \tag{14}$$

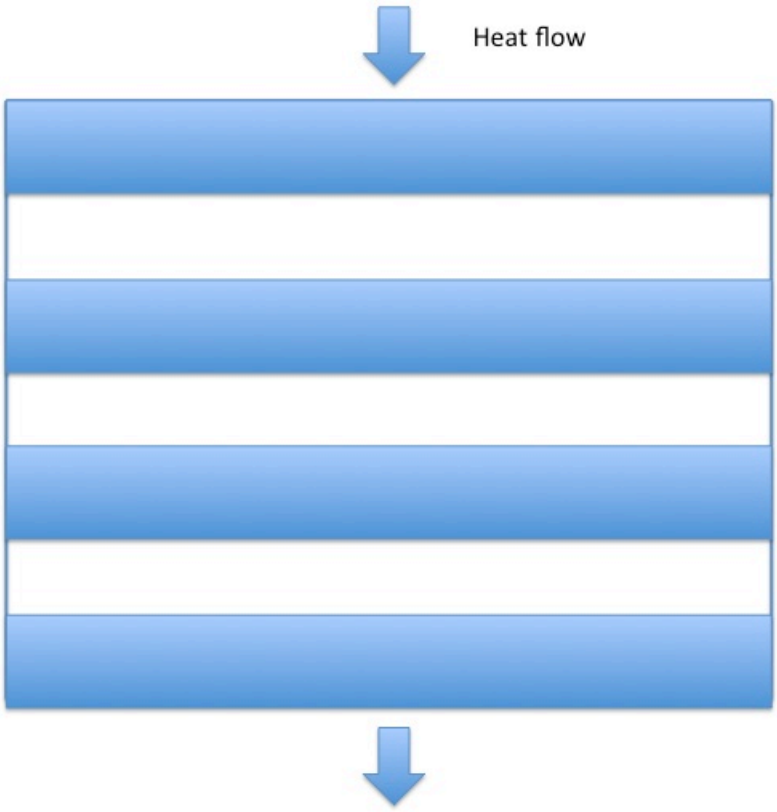

Figure 8. Schematic diagram for series model

3. Series parallel model [27]

The series parallel model in Figure 9 is a combination of the series model and parallel model:

$$k = \frac{1}{\frac{\omega_{parallel}}{k_{parallel}} + \frac{\omega_{series}}{k_{series}}} \tag{15}$$

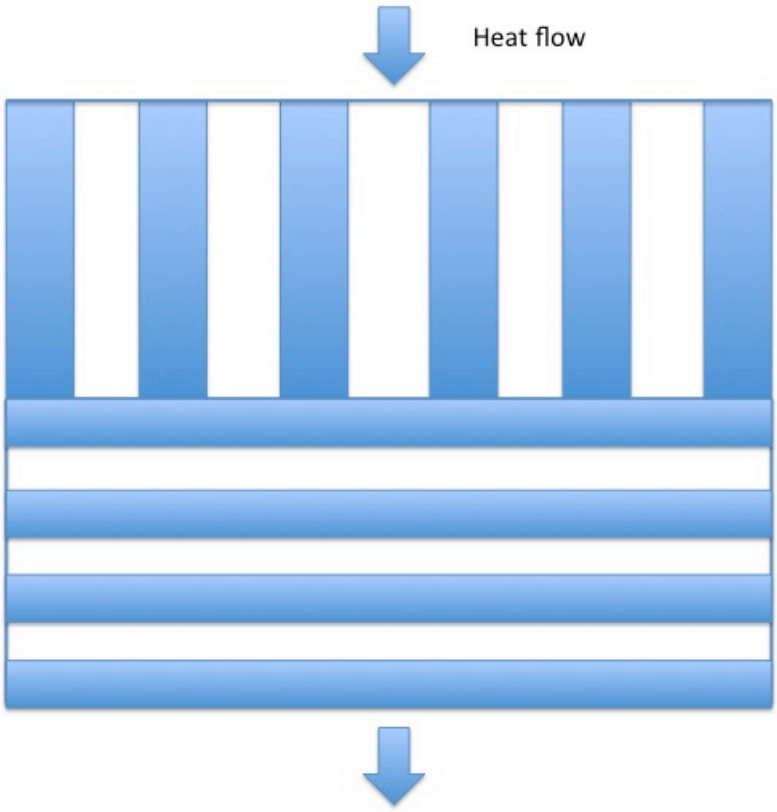

Figure 9. Schematic diagram for series parallel model

4. Maxwell Eucken model [27]

The Maxwell Eucken model in Figure 10 assumes dispersed particles are isolated in the material that will never connect with each other during heat conduction:

$$k = k_1 \frac{2k_1 + k_2 - 2(k_1 - k_2)\xi_2}{2k_1 + k_2 + 2(k_1 - k_2)\xi_2} \tag{16}$$

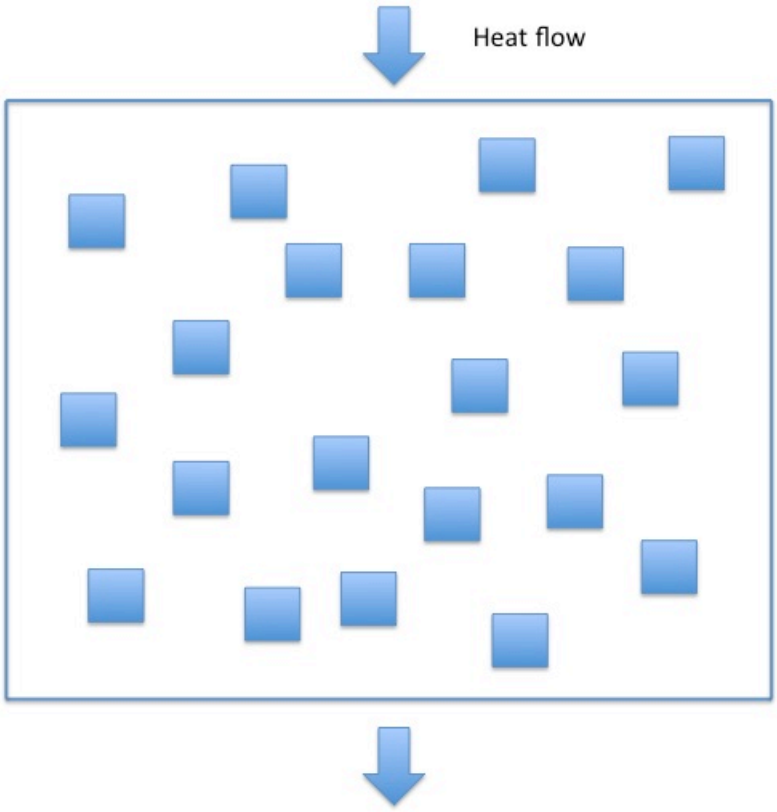

Figure 10. Schematic diagram for Maxwell Eucken model

5. Effective Medium Theory [27]

The Effective Medium Theory in Figure 11 assumes both components are stochastically distributed in the material:

$$k = \frac{1}{4}\{(3\xi_2 - 1)k_2 + [3(1-\xi_2)-1]k_1 + \sqrt{[(3\xi_2 - 1)k_2 + (2-3\xi_2)k_1]^2 + 8k_1k_2}\} \quad (17)$$

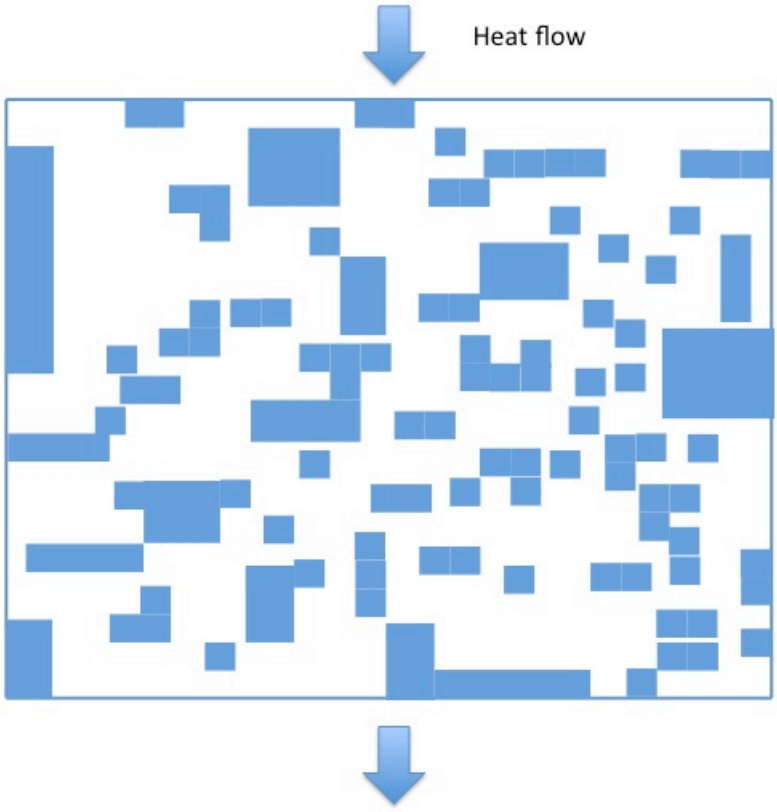

Figure 11. Schematic diagram for Effective Medium Theory

Objectives

Various experimental approaches have been employed to measure thermal conductivity of dry unsaturated DM [28-33] . Khandelwal and Mench [30] measured carbon paper and Nafion® membranes for PEFCs. They reported that Sigracet® 20 wt.% PTFE treated carbon paper had a thermal conductivity of

0.22±0.04 W/m/K and Toray paper had a thermal conductivity of 1.80±0.27 W/m/K. Burheim et al. [31] reported an increase of thermal conductivity of artificially aged SGL gas diffusion media while PTFE content decreases. They also measured SolviCore DM at different compression pressures. They reported that thermal conductivity increases as compression pressures grow and an increase in thermal conductivity when the DM is saturated [32]. Zamel et al. [28] measured the through-plane thermal conductivity of dry Toray paper in a temperature range from -50°C to 120°C. A thermal conductivity of 0.8 to 1.8 W/m/K was reported at high compression, and 0.2 to 0.4 W/m/K at low compression.

Several researchers also proposed numerical models to calculate thermal conductivity of DM [8,10,27]. However, measurement of the thermal conductivity of diffusion media as a function of both compression and saturation has not yet been fully developed so that the impact on transport can be fully understood, and is the motivation for this study.

In this study, measurements of stress-strain relationship and thermal conductivity as a function of saturation were performed. A theoretical analysis of the maximum thermal conductivity as a function of saturation has been developed to glean insight into the internal distribution and connectivity of liquid in the media. The results of this work should be useful to understand and more precisely model thermal transport in operating PEFCs with realistic saturation distributions.

CHAPTER III

EXPERIMENTAL SETUP AND PROCEDURE

Experimental Setup

Diffusion media were uniformly compressed between two 25mm thick stainless steel cylinders with known thermal conductivity. This design enabled determination of the stress-strain relationship and the through-plane thermal conductivity. The schematic diagrams of the experimental apparatus were shown in Figure 12 and Figure 13. A load cell was used to measure compression pressure on diffusion media. All tests were performed at room temperature (21 - 27°C).

Design and Instrumentation

A Hot Disk TPS2500S Thermal Constants Analyser was used to non-destructively measure the thermal conductivity of all materials tested in this work. Based on the theory of the Hot Disk Transient Plane Source (TPS) technique, a TPS sensor in the shape of a double spiral was utilized to take measurements within ten seconds effectively decreasing unwanted water vaporization during the tests.

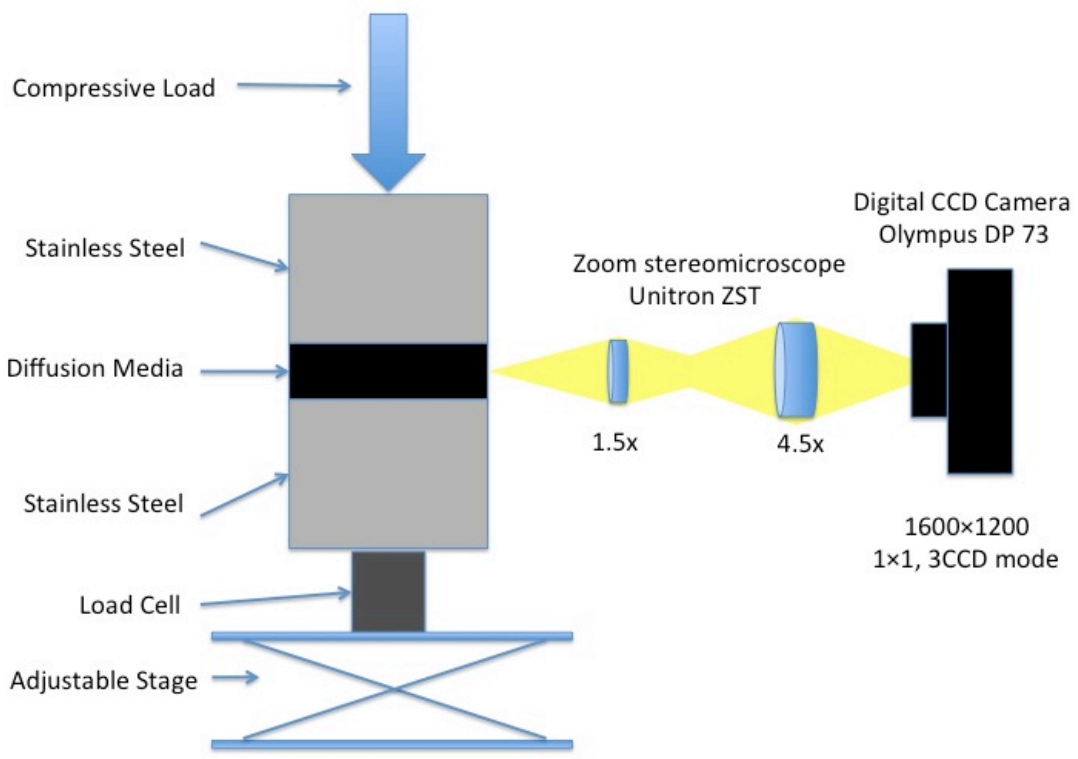

Figure 12. Schematic diagram of the experimental apparatus to optically measure the developed stress-strain relationship of thin film materials (Not to scale)

The TPS sensor acted both as a heat source for increasing the temperature of the samples and a “resistance thermometer” for recording the time dependent temperature increases[34]. The reproducibility of measured thermal conductivity using this technique was 3%.

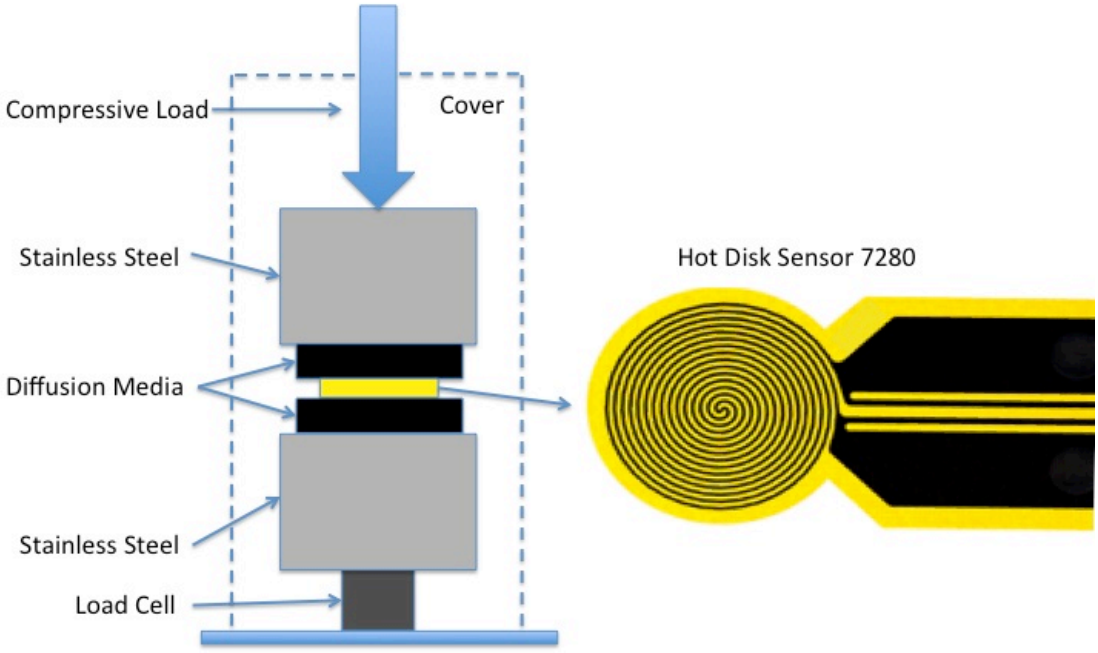

Figure 13. Schematic diagram of the experimental apparatus to measure thermal conductivity of thin film materials (Not to scale)

DM Thickness Measurement

Round, 53 mm diameter samples were used for stress-strain measurement. Mitsubishi Rayon Corp. Grafil U-105 (MRC 105), SGL Sigracet® 25 BC, Auto-Competitive samples were used in this study. Auto-Competitive samples are the materials that satisfy the 2015 USDOE performance targets while enabling progress toward the automotive fuel cell system cost target of

$30/kWe. To increase the measured deflection, two samples of MRC 105, SGL 25 BC, or Auto-Competitive (AC) were layered for each stress-strain measurement. Images of compressed samples were captured using a zoom stereomicroscope (Unitron ZST) and digital CCD camera (Olympus DP 73) with optical resolution of 1600×1200 pixels. Deflections of the DM in the images were measured using digital imaging software cellSens Standard.

The DM stress-strain relationship was optically measured, as shown in Figure 14. The thickness versus compression relationship was then used to calculate the thickness used in the determination of thermal conductivity.

Porosity is of great importance to control and calculate saturation of porous media. As compression increased, the void volume in DM was reduced, hence decreasing porosity according to the following equation:

$$\phi^* = 1 - \frac{1-\phi}{1-\varepsilon} \tag{18}$$

where ϕ^* is the compressed porosity of DM, ϕ is the initial porosity of DM, and ε is the total strain on the compressed DM. It should be noted that during compression to 2 MPa, the MPL is generally incompressible, so that the load deformation can be considered on the DM only.

Table 2 shows initial porosity and compressed porosity of three different diffusion media under 2 MPa compression.

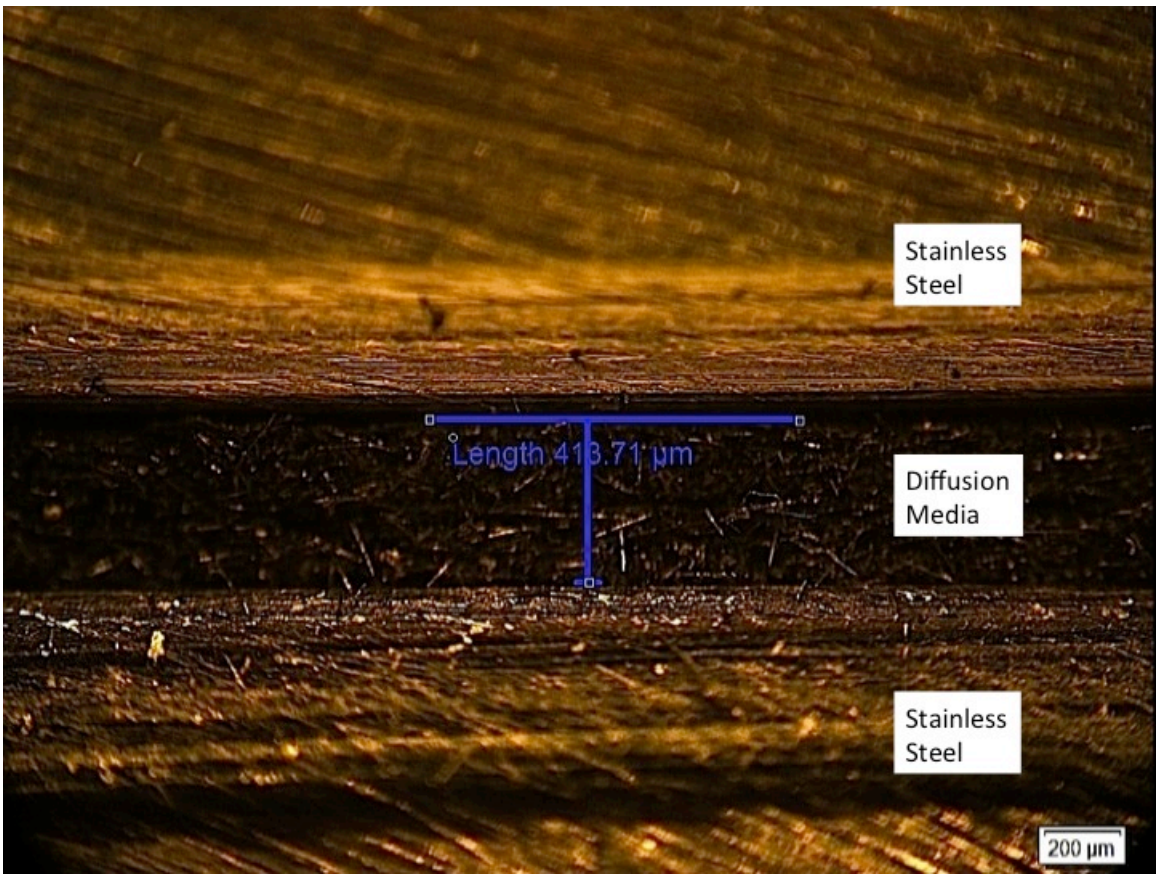

Figure 14. Photograph of a DM under compression in microscope

Experimental Procedure

Saturation of the diffusion media

Dry weight and thickness were measured prior to the saturation process. In this study, porous diffusion media were artificially saturated by immersion in de-ionized (DI) water in a sealed container while a vacuum was applied.

Immersion in a sonic bath was utilized to detach residual bubbles during saturation[35]. The thickness under 2 MPa compression was calculated based on the stress strain relationship and the following equation:

$$l = l_0 \frac{1-\varepsilon}{1-\varepsilon_0} \tag{19}$$

where l is the thickness of compressed DM, l_0 is the thickness of measured DM, ε is the total strain on compressed DM, ε_0 is the strain on measured DM.

The wet weight of diffusion media were calculated prior to saturation based on the following equation:

$$m_{wet} = m_{dry} + s\rho_{water} A l \phi^* \tag{20}$$

where m_{wet} and m_{dry} are weight of wet and dry diffusion media, respectively, s is the saturation of DM, ρ_{water} is the density of water, A is the area of DM, l is the thickness of the compressed DM, ϕ^* is the compressed porosity of the DM.

For MRC 105 DM, without MPL, the thickness of the DM l_1 is the thickness of compressed DM. For Auto-Competitive DM shown in Figure 15g, with thin MPL, the thickness of the compressed macroporous layer was almost the same as the thickness of compressed DM since the MPL was relatively thinner than macroporous layer. For SGL 25 BC, with thick MPL, the thickness of the compressed macroporous layer was used to calculate saturation instead of the thickness of compressed DM since MPL was assumed to be unsaturated. The ratio between the thickness of the compressed macroporous layer and the

thickness of the compressed DM will be discussed in the model. The compressed porosity of DM was calculated as shown Table 2.

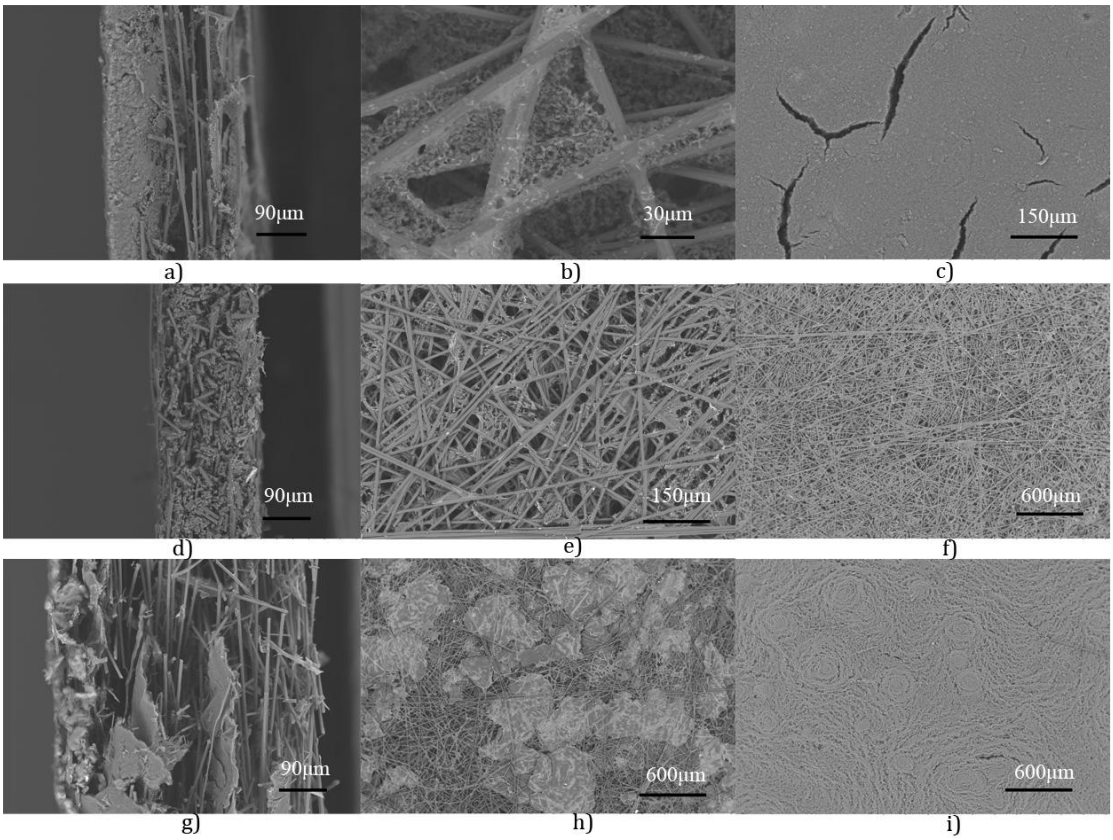

Figure 15. SEM images a) SGL 25 BC cross section b) SGL 25 BC face of macroporous layer c) SGL 25 BC face of MPL d) MRC 105 cross section e) MRC 105 face of macroporous layer f) MRC 105 face of macroporous layer g) Auto-Competitive cross section h) Auto-Competitive face of macroporous layer i) Auto-Competitive face of MPL

Table 2. Calculated change in porosity under 2MPa compression

DM	*Initial porosity*	*Updated porosity*
Auto-Competitive	82.0%	67.8%±1.2%
SGL 25 BC	80.0%	64.8%±0.7%
MRC 105	83.2%	79.1%±0.2%

Since some water is squeezed out of the diffusion media during compression loading, the average decrease in saturation during compression loading was calculated and compensated prior to saturation. After each test series, an updated wet weight was immediately measured. Saturation was calculated based on the following equation:

$$s = \frac{m_{wet} - m_{dry}}{\rho_{water} A l \phi^*} \tag{21}$$

Dry and Saturated DM Thermal Conductivity Measurement

Thermal conductivity was measured by the application of through-plane test module. Two specimens were required for each test. As shown in Figure 13, one sample was placed above the Hot Disk sensor. The other was placed underneath the sensor. All of them were firmly clamped together between two 25mm thick stainless steel cylinders with known high thermal conductivity. For

dry measurements, samples were consecutively tested under 0.1MPa, 0.5MPa, 1MPa, 1.5MPa and 2MPa compressions. Thirty minutes of time delay were taken before each test. Transient measurement time was set at 10 seconds. Heating power was 2.2 watts. The ambient temperature in this study varied from 21°C to 27°C, which should not make a significant impact on results based on previous studies[30].

In the experiments for determination of saturated DM thermal conductivity, the compression pressure was set at 2MPa, which is in the normal range of fuel cell assembly. Samples were saturated to a higher saturation level and tested when target weights were reached. At least thirty minutes before each test was needed to insure that experiment was carried out at steady state conditions.

Measurement Validation

The thickness measurement was validated with a stage micrometer for transmitted light (Ted Pella, Inc.). The thickness measured was 1.89% lower than the actual value, which is within the expected experimental uncertainty.

Thermal measurement was validated with a thin disk of Teflon® PTFE, SGL 25 BC DM and stainless steel. The measured PTFE thermal conductivity was determined to be 0.240±0.025 W/m/K compared to the Teflon® PTFE standard thermal conductivity of 0.259±0.006 W/m/K. The measured SGL 25 BC

thermal conductivity was 0.214±0.004 W/m/K under 0.5MPa compression and 0.356±0.018 W/m/K under 1MPa compression. Ramousse et al.[11] reported a thermal conductivity of 0.26~0.34 W/m/K. Khandelwal and Mench[30] reported thermal conductivity of 0.31±0.06 W/m/K. The measured stainless steel thermal conductivity was 13.380±0.036 W/m/K. Hot Disk AB reported an average thermal conductivity of 13.7418 W/m/K with less than 0.15% standard deviation based on these results, the test system was deemed to be within acceptable limits of precision.

CHAPTER IV

RESULTS AND DISCUSSION

This chapter discusses the results from SEM images, thickness measurement of DM. Thermal conductivity measurement of dry and saturated DM were performed. Thermal conductivity maximum prediction of saturated DM as a function of both compression and saturation were performed.

SEM Images

The characteristic structures of the cross-section, the face of the macro porous layers and the face of the micro porous layers are shown in Figure 15 using scanning electron micrographs (HITACHI TM3000).

The micrographs showed that SGL 25 BC, MRC 105 and Auto-Competitive DM primarily have planar structures of fibers aligned in multiple layers. The presence of PTFE can be observed between the fibers. SGL 25 BC has a relatively thick MPL (46% of DM thickness), which was essentially incompressible under the loads experiment in testing. Nevertheless, Auto-Competitive samples have much thinner MPL that was negligible in this study, and MRC 105 samples don’t have MPL. In the Auto-Competitive DM, carbon-fiber skeleton filled with carbon powder was observed as shown in Figure 15.

DM Thickness Measurement

Figure 16 presents three fitting curves of the measured stress-strain deflection for Auto-Competitive, SGL 25 BC and MRC 105.

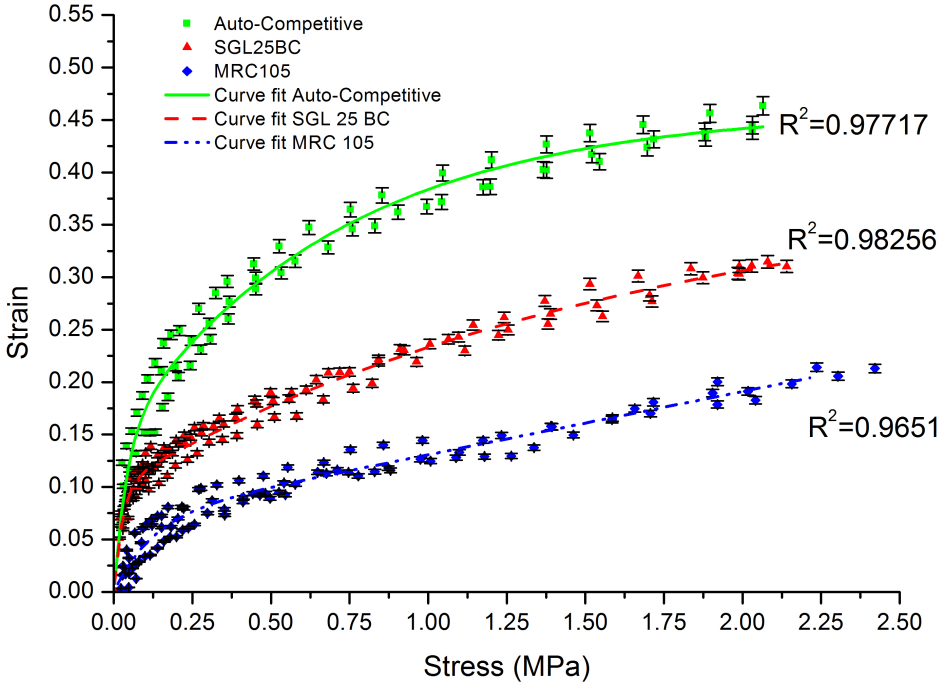

Figure 16. Experimental data and curve fit lines for measured stress strain relationships

The stress-strain relationship for the DM is essential for thermal conductivity measurements. For Auto-Competitive DM, the strain sharply increased 15% during initial compression loading (0.1MPa) and nonlinearly approached to 44.1% under 2MPa compression. The effective compressed

porosity is lowered from 82.0% to 67.8% during compression to 2 MPa. For SGL 25 BC MPL, the total strain was calculated to be 4.9%. For SGL 25 BC macroporous layer, 10% strain was reached during the initial compression loading, and approached to 30.6% resulting in lowering porosity from 80.0% to 64.8%. MRC 105 didn't have much strain as other materials during the initial compression loading. After having 9% deflection under 0.25MPa compression, MRC 105 began to deflect linearly up to 19.5% under 2MPa compression. A nonlinear curve fitting was performed using an exponential association model:

$$Y = a_1(1 - e^{-\frac{x}{b_1}}) + a_2(1 - e^{-\frac{x}{b_2}}) \quad (22)$$

Table 3 and Figure 16 show the three experimental stress-strain curve fitting models of Auto-Competitive, SGL 25 BC and MRC 105, respectively.

A residual strain was observed when the compressive load was released due to plastic deformation. In this study, the focus was thickness measurement and prediction and thermal conductivity measurements were only performed on virgin materials under initial compression. Therefore, successive compress-release cycles were not performed.

Table 3. Stress-strain curve fitting functions

DM	*Experimental stress-strain curve fitting functions*
Auto-Competitive	$\varepsilon = 0.14429(1 - e^{-\frac{\sigma}{0.04031}}) + 0.31607(1 - e^{-\frac{\sigma}{0.70534}})$
SGL 25 BC	$\varepsilon = 0.29558(1 - e^{-\frac{\sigma}{1.68126}}) + 0.10073(1 - e^{-\frac{\sigma}{0.02651}})$
MRC 105	$\varepsilon = 0.07055(1 - e^{-\frac{\sigma}{0.12226}}) + 1.79812 * 10^{8}(1 - e^{-\frac{\sigma}{2.98335*10^{9}}})$

Thermal Conductivity Measurement of Dry Samples

Figure 17 shows measured thermal conductivity of dry DM under various compressions up to and 2 MPa. Thermal conductivity was relatively low when low compression pressure was applied because of the presence of the internal contact resistance and high porosity in the DM. With increased compression, internal contact resistance and porosity decreases. Hence, measured thermal conductivity of the DM increases. The thermal conductivity of dry Auto-Competitive monotonically increases with respect to compression pressure from 0.1 MPa to 2 MPa by 440%. The measured thermal conductivity increased about 80% when compression pressure varied from 1.0 MPa to 1.5 MPa. Since the strain almost reached the maximum points, carbon powder and carbon fiber were more likely connected with each other reducing internal conductive resistance

and forming new heat transfer pathways. Thermal conductivity of dry SGL 25 BC and MRC 105 linearly increased with respect to compression loading. Repeatability of those two DM was higher than Auto-Competitive ones.

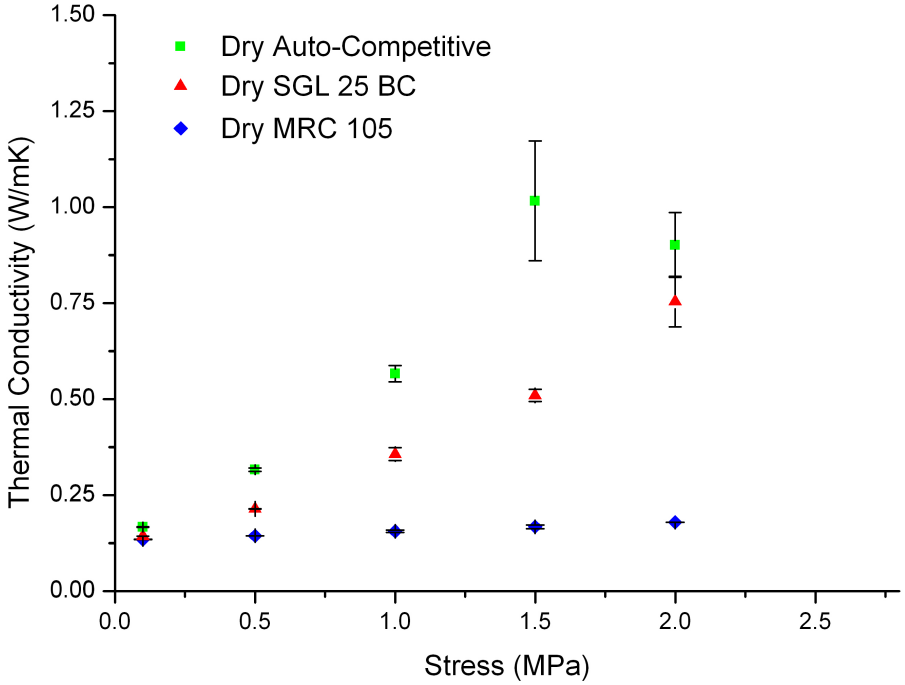

Figure 17. Measured thermal conductivity of dry DM as a function of compression

Thermal Conductivity Measurement of Saturated Samples

Figure 18 presents measured and predicted maximum thermal conductivity of saturated Auto-Competitive, SGL 25 BC and MRC 105 DM under 2 MPa compression.

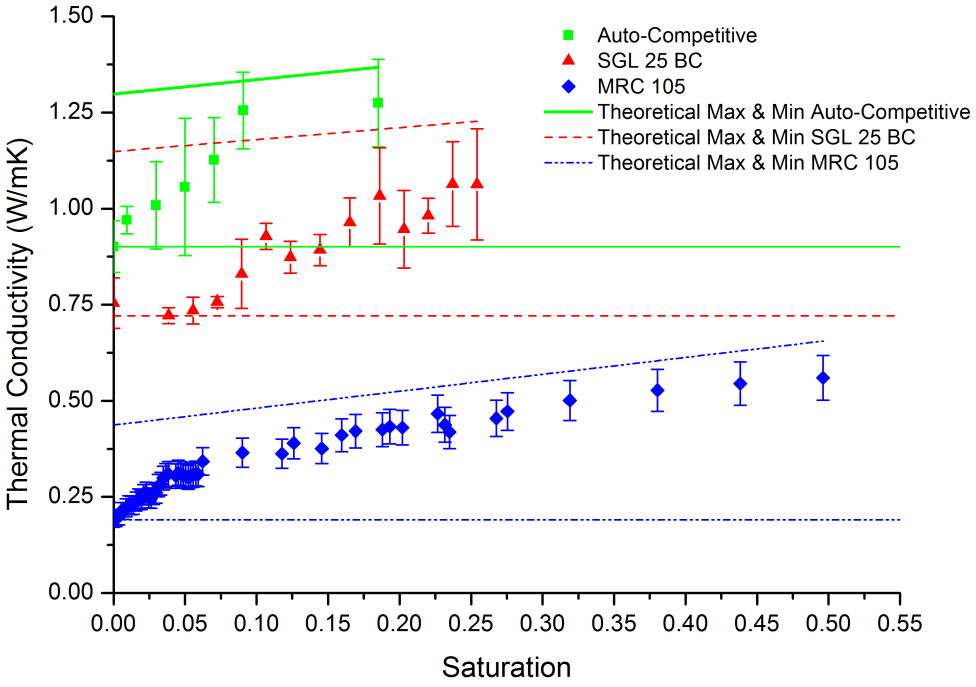

Figure 18. Measured and predicted maximum thermal conductivity as a function of saturation for various DM at 2.0 MPa compression

As expected, water content had a significant effect on the increment of thermal conductivity of DM. Thermal conductivity of MRC 105 sharply increased nearly 62% from 0 to 6% saturation and gradually approached to theoretical maximum as saturation levels increased. The theoretical maximum shown was developed from analytical parallel model that was derived. The Auto-Competitive DM were more easily saturated comparing to MRC105. As shown in Figure 18, water content obtained in Auto-Competitive samples had an obvious influence on thermal conduction with saturation from 0 to 10%. Similar to MRC 105, the

thermal conductivity of SGL 25 BC gradually increased 35% as saturation levels increased from 0 to 25%.

Theoretical maximum prediction of thermal conductivity using parallel model and series-parallel model

It is well known that DM used in PEFC is a heterogeneous material with carbon fibers or cloth and heat conduction is a dominant heat transfer mode through the DM. Many models have been described in literature[8,9,12,27,36,37] to predict the thermal conductivity of porous diffusion media. But saturation was not considered in those models, primarily due to lack of experimental data now available.

A simplified model was developed in this study with basic components (carbon, water and air) connected, and parallel to the heat flow, as shown in Figure 19.

This represents the theoretical maximum of thermal conductivity of porous diffusion media at 2 MPa compression, if all saturation was connected and aligned.

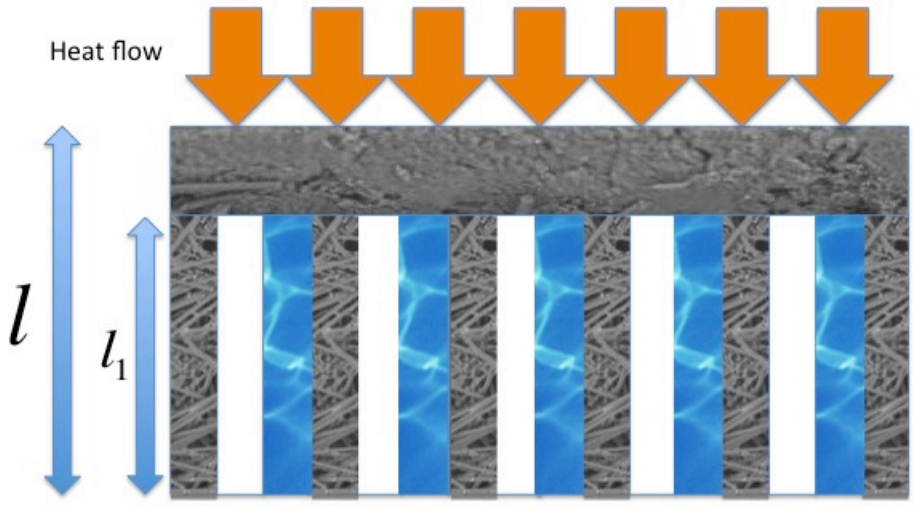

Figure 19. Illustration of theoretical maximum thermal conductivity of saturated porous diffusion media

$$k_1 = \phi^*(k_w - k_a)s + (1-\phi^*)k_c + \phi^* k_a \tag{23}$$

$$k_2 = k_c \tag{24}$$

$$k = \frac{l}{\frac{l_1}{k_1} + \frac{l - l_1}{k_2}} \tag{25}$$

For SGL 25 BC:

$$k = \frac{4.12232s + 8.22939}{s + 8.68781} \tag{26}$$

For MRC 105:

$$k = 0.4398s + 0.437 \tag{27}$$

For Auto-Competitive:

$$k = 0.376968s + 1.29783 \tag{28}$$

where k_w is the thermal conductivity of water, k_c is the thermal conductivity of carbon material, k_c is the thermal conductivity of air, l_1 is the thickness of compressed macroporous layer, and l is the thickness of compressed DM.

Table 4. Material properties

DM	ϕ^* ***(%)***	k_w ***(W/m/K)***	k_c ***(W/m/K)***	k_a ***(W/m/K)***	l_1 / l
SGL 25 BC	64.8	0.58	1.7	0.024	0.412
MRC 105	79.1	0.58	1.7	0.024	1
AC	67.8	0.58	3.98	0.024	≈ 1

The theoretical maximum thermal conductivity prediction was presented in Figure 18. A significant difference between measured dry thermal conductivity and theoretical maximum was observed, since the planar structures of the fibers in all of three DM are orthogonal to the direction of heat flow. At low saturation, water droplets began to connect multiple fibers among different sub-layers to

create connected heat transfer pathways. As saturation increases, multiple pores were filled up with water forming connected heat conduction pathways, approaching theoretical limits.

Theoretical maximum thermal conductivity as a function of both compression and saturation

The compressed porosity is a function of strain, and strain is a function of compression, therefore compressed porosity can be described as a function of compression.

Substituting Equation 18 in Equation 23 yields:

$$k_1 = (1 - \frac{1-\phi}{1-\varepsilon^*})[(k_w - k_a)s - k_c + k_a] + k_c \quad (29)$$

For SGL 25 BC:

$$\phi = 0.800, \frac{l_1}{l} = \frac{1-\varepsilon^*}{1-\varepsilon} \times (1 - 46\%) \quad (30)$$

$$\varepsilon^* = 0.1427(1 - e^{-\frac{\sigma}{0.1}}) + 1.88643 * 10^{13}(1 - e^{-\frac{\sigma}{1.30697*10^{14}}}) \quad (31)$$

For MRC 105:

$$\phi = 0.832, l_1 = l, \varepsilon^* = \varepsilon \quad (32)$$

For Auto-Competitive:

$$\phi = 0.820, l_1 \approx l, \varepsilon^* = \varepsilon \tag{33}$$

where ε^* is the strain on macroporous layer, ϕ is the initial porosity of DM.

Substituting Equation 24, 25, 30, and 31 in Equation 29, theoretical maximum prediction of thermal conductivity for SGL 25 BC was solved:

$$k = \frac{85(\varepsilon - 1)(695\varepsilon^* s + 30\varepsilon^* - 556s - 449)}{\Sigma} \tag{34}$$

where

$$\Sigma = 106250\varepsilon^2 + 34750\varepsilon\varepsilon^* s - 162125\varepsilon\varepsilon^* - 27800\varepsilon s - 14000\varepsilon - 18765(\varepsilon^*)^2 s + 113940(\varepsilon^*)^2 + 17792\varepsilon^* s - 110980\varepsilon^* - 2224s + 55575$$

Substituting Equation 24, 25, and 32 in Equation 29, theoretical maximum prediction of thermal conductivity for MRC 105 was solved:

$$k = \frac{0.556\varepsilon s + 0.024\varepsilon - 0.462592s - 0.305568}{\varepsilon - 1} \tag{35}$$

Substituting Equation 24, 25, and 33 in Equation 29, theoretical maximum prediction of thermal conductivity for Auto-Competitive was solved:

$$k = \frac{0.556\varepsilon s + 0.024\varepsilon - 0.462592s - 0.73608}{\varepsilon - 1} \tag{36}$$

Figure 20 illustrated the theoretical maximum prediction of thermal conductivity as a function of both compression and saturation.

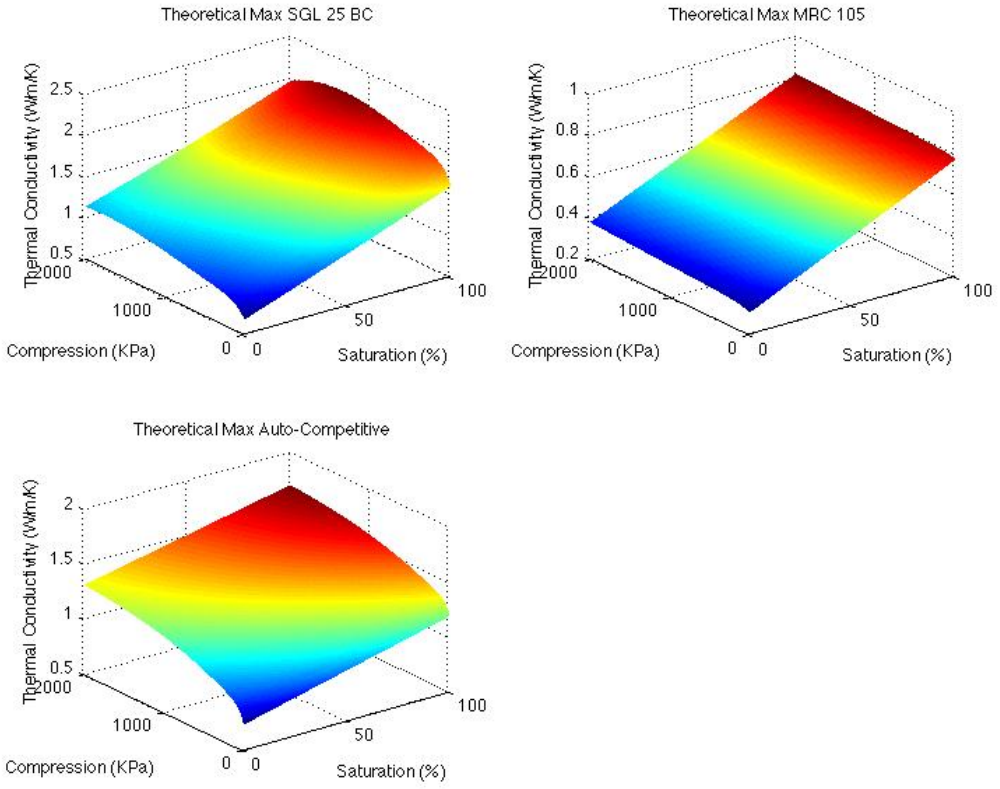

Figure 20. Theoretical maximum prediction of thermal conductivity as a function of both compression and saturation

CHAPTER V

CONCLUSIONS AND RECOMMENDATIONS

The objective of this study was to investigate the relationship of thermal conductivity with compression and saturation in three representative fuel cell diffusion media and to estimate temperature drop in an operating polymer electrolyte fuel cell. The stress-strain relationship of the materials was measured using an optical microscopic technique. The through-plane thermal conductivity of diffusion media was found to be highly dependent on the compression and the water content, and expressions relating saturation and compression to thermal conductivity and compression of the media were developed. Additionally, a theoretical prediction of the maximum through-plane thermal conductivity was developed as a function of both compression and saturation to understand the nature of liquid connectivity in saturated pores. The results of this study should be useful to improve predictions of the internal temperature gradients and transport phenomenon inside the PEFCs.

Measurement of thickness is critical to determine compressed porosity and thermal conductivity. Nonlinear sharp increase in strain at initial compressive loading was observed.

Measured and predicted maximum thermal conductivity as a function of saturation for various DM at 2MPa compression pressure was performed. There was a significant increase in thermal conductivity with an increase in saturation.

Moving forward, future work could include the measurement of thermal conductivity of DM with different saturation at a large range of temperature to develop a thermal conductivity model as a function of compression, saturation and temperature to better estimate the internal temperature distribution in PEFCs under different operating conditions.

Moreover, testing thermal conductivity of DM with ice content could be helpful for PEFCs applications, especially fuel cell vehicles under cold operating conditions.

LIST OF REFERENCES

[1] M.M. Mench, Fuel Cell Engines, John Wiley&Sons, Inc, Hoboken, New Jersey, 2008.
[2] S.G. Kandlikar, Z. Lu, Journal of Fuel Cell Science and Technology, 6 (2009) 044001.
[3] K.M. Yin, C.P. Chang, Fuel Cells, 11 (2011) 888-896.
[4] M.F. Mathias, J. Roth, J. Fleming, W. Lehnert, Handbook of Fuel Cells-Fundamentals, Technology and Applications, in: John Wiley & Sons, 2003.
[5] S. He, M.M. Mench, Journal of The Electrochemical Society, 153 (2006) A1724.
[6] Y. Shi, J. Xiao, S. Quan, M. Pan, R. Yuan, Journal of Power Sources, 185 (2008) 241-247.
[7] D. Veyret, G. Tsotridis, Journal of Power Sources, 195 (2010) 1302-1307.
[8] J. Wang, J.K. Carson, M.F. North, D.J. Cleland, International Journal of Heat and Mass Transfer, 49 (2006) 3075-3083.
[9] J. Wang, J.K. Carson, M.F. North, D.J. Cleland, International Journal of Heat and Mass Transfer, 51 (2008) 2389-2397.
[10] J. Yablecki, A. Nabovati, A. Bazylak, Journal of The Electrochemical Society, 159 (2012) B647.
[11] J. Ramousse, S. Didierjean, O. Lottin, D. Maillet, International Journal of Thermal Sciences, 47 (2008) 1-6.
[12] E. Sadeghi, M. Bahrami, N. Djilali, Journal of Power Sources, 179 (2008) 200-208.
[13] E. Sadeghi, N. Djilali, M. Bahrami, Journal of Power Sources, 196 (2011) 246-254.
[14] N. Zamel, X. Li, J. Shen, J. Becker, A. Wiegmann, Chemical Engineering Science, 65 (2010) 3994-4006.
[15] C.Y. Wang, Chem. Rev., 104 (2004) 4727-4766.
[16] H. Ju, C.-Y. Wang, S. Cleghorn, U. Beuscher, Journal of The Electrochemical Society, 152 (2005) A1645.
[17] S. Tsushima, K. Teranishi, S. Hirai, Electrochemical and Solid-State Letters, 7 (2004) A269.
[18] W.-M. Yan, F. Chen, H.-Y. Wu, C.-Y. Soong, H.-S. Chu, Journal of Power Sources, 129 (2004) 127-137.
[19] T.E. Springer, T.A. Zawodzinski, S. Gottesfeld, Journal of The Electrochemical Society, 138 (1991) 2334-2342.
[20] P.A. Chuang, A. Turhan, A.K. Heller, J.S. Brenizer, T.A. Trabold, M.M. Mench, in: The Third International Conference on Fuel Cell Science, Engineering and Technology, 2005.
[21] A. Bazylak, D. Sinton, Z.S. Liu, N. Djilali, Journal of Power Sources, 163 (2007) 784-792.
[22] J.B. Ge, A. Higier, H.T. Liu, Journal of Power Sources, 159 (2006) 922-927.

[23] W.J. Parker, R.J. Jenkins, C.P. Butler, G.L. Abbott, Journal of Applied Physics, 32 (1961) 1679.
[24] R.D. Cowan, Journal of Applied Physics, 34 (1963) 926.
[25] J.A. Cape, G.W. Lehman, Journal of Applied Physics, 34 (1963) 1909.
[26] J. Zajas, P. Heiselberg, International Journal of Heat and Mass Transfer, 60 (2013) 542-548.
[27] J.K. Carson, S.J. Lovatt, D.J. Tanner, A.C. Cleland, International Journal of Heat and Mass Transfer, 48 (2005) 2150-2158.
[28] N. Zamel, E. Litovsky, X. Li, J. Kleiman, International Journal of Hydrogen Energy, 36 (2011) 12618-12625.
[29] G.S. Hwang, A.Z. Weber, Journal of The Electrochemical Society, 159 (2012) F683-F692.
[30] M. Khandelwal, M.M. Mench, Journal of Power Sources, 161 (2006) 1106-1115.
[31] O.S. Burheim, G. Ellila, J.D. Fairweather, A. Labouriau, S. Kjelstrup, J.G. Pharoah, Journal of Power Sources, 221 (2013) 356-365.
[32] O. Burheim, P.J.S. Vie, J.G. Pharoah, S. Kjelstrup, Journal of Power Sources, 195 (2010) 249-256.
[33] G. Karimi, X. Li, P. Teertstra, Electrochimica Acta, 55 (2010) 1619-1625.
[34] J.S. Gustavsson, Gustavsson, M., Gustafsson, S.E., Thermal Conductivity 24, (1997) 116-122.
[35] K.T. Cho, M.M. Mench, Journal of Power Sources, 195 (2010) 3858-3869.
[36] J.K. Carson, S.J. Lovatt, D.J. Tanner, A.C. Cleland, Journal of Food Engineering, 75 (2006) 297-307.
[37] S.R. Jagjiwanram, Applied Thermal Engineering, 24 (2004) 2727-2735.

VITA

Guoqing Xu was born on November 13, 1986. He grew up in Linping, Yuhang District, Hangzhou City, China. He went to Yuhang High School. He then went to study Biomedical Engineering at Central South University in Changsha. He graduated with a Bachelor's Science in June of 2009. He went to intern in Chinese Academic of Sciences-Max Planck Gesellschaft Partner Institute for Computational Biology, Shanghai, China from August to September of 2008. He began her graduate study in August of 2010. He will graduate with his Master of Science in mechanical engineering in May of 2013.